



Photocatalytic paper based on sol-gel titania nanoparticles immobilized on porous silica for VOC abatement



S. Adjimi^{a,b}, N. Sergent^{a,b}, J.-C. Roux^{a,b}, F. Delpech^{a,b}, M. Pera-Titus^{d,e}, K. Chhor^c, A. Kanaev^c, P.-X. Thivel^{a,b,*}

^a Université Grenoble Alpes, LRP, LEPMI, LGP-2, F-38000 Grenoble, France

^b CNRS, LRP, LEPMI, LGP-2, F-38000 Grenoble, France

^c Laboratoire des Sciences des Procédés et des Matériaux, CNRS, Université Paris 13, Sorbonne Paris Cité, 93430 Villetaneuse, France

^d Université de Lyon, Institut de Recherches sur la Catalyse et l'Environnement de Lyon (IRCELYON), UMR 5256 CNRS-UCBL1, 2 Av Albert Einstein, 69626 Villeurbanne, France

^e Eco-Efficient Products and Processes Laboratory (E2P2L), UMI 3464 CNRS-Rhodia, 3066 Jin Du Road, Xin Zhuang Ind. Zone, 201108 Shanghai, China

ARTICLE INFO

Article history:

Received 8 November 2013

Received in revised form 2 February 2014

Accepted 7 February 2014

Available online 16 February 2014

Keywords:

Photocatalysis

Paper

Ethanol

Silica

Sol-gel

ABSTRACT

A new composite paper with high photocatalytic performance has been successfully manufactured by introducing titania-anchored porous silica into cellulose fibres. The silica particles with an average size of 700 nm were synthesized via CaCO_3 templating and further employed as support to grow titania nanoparticles (5.2 nm) by sol-gel synthesis with variable weight ratios. The photocatalytic materials have been characterized using various techniques including BET, XRD, Raman spectroscopy, SEM and TEM + EDX + ED microscopies. The composite $\text{TiO}_2/\text{SiO}_2$ particles have been further introduced in bulk paper to generate highly active photocatalytic TiO_2 -loaded papers. The activity of the papers has been demonstrated in the room-temperature degradation of ethanol (50–200 ppm) under UV irradiation, showing a comparable activity to that of commercial TiO_2 -coated papers. The effect of the main textural variables during papermaking on the photocatalytic performance are discussed in detail.

© 2014 Elsevier B.V. All rights reserved.

1. Introduction

Air pollution remediation ascribed to volatile organic compounds (VOCs) is a major challenge facing industrialized and emerging countries at present. VOCs are organic chemicals (in particular odours and scents) characterized by a high vapour pressure at near-room temperature ($>0.01 \text{ kPa}$ at 20°C) according the EU Directive 1999/13/CE and the further amendment [1,2]), favouring their transfer from the liquid/solid emission source to the surrounding air. Atmospheric VOCs can be generated either naturally due to biogenic activity (emissions from biomass and fermentations), or through man-made activities ascribed to transport (14%), housing (37%), and industrial transformations (36%) [3]. VOCs can also act as precursors of secondary pollutants such as tropospheric ozone by photochemical reaction with NO_x [4]. Finally, VOCs can be emitted to indoor air environments by the use of daily products and

consumables such as perfumes, cosmetics, paintings, magazines, and tobacco.

VOCs can have a direct and long-term impact on human health. Exposition to VOCs can cause skin irritation, rhinitis, headache, fatigue, and allergic reactions among other effects [5,6]. Besides, some VOCs derived from aromatic molecules or trichloroethylene (TCE) can show carcinogenic and mutagenic activity on humans [7]. The intrinsic hazard of VOCs to public health has motivated the development of technologies aiming at their removal and abatement from open and indoor air environments.

The available technologies for VOC remediation include physicochemical methods (e.g., adsorption on activated carbons and zeolites, condensation, membrane separation) [8], and destructive methods such as bio-filtration [9], thermal incineration [10], non-thermal plasma catalysis [11], and catalytic combustion [12,13]. On the one hand, bio-filtration is strongly limited by the temperature and the toxicity of the pollutants towards the microorganisms, as well as by the uncontrolled growth of biomass leading to the obstruction of biofilters. On the other hand, incineration is highly energy intensive ($800\text{--}1200^\circ\text{C}$) and can involve the generation of dioxins and NO_x , being discouraged for the treatment of flowrates

* Corresponding author.

E-mail address: pierre-xavier.thivel@ujf-grenoble.fr (P.-X. Thivel).

with VOCs at low-to-moderate concentrations. Finally, even if catalytic combustion can reduce the incineration temperatures down to 200–300 °C, the technique usually requires expensive noble metals supported on oxides.

Photocatalysis emerges as an alternative technology to reduce VOC concentration at near room [14,15]. In this technique, a semiconductor photocatalyst is irradiated in the presence of water vapour and an electron acceptor (usually atmospheric oxygen). Titanium dioxide (TiO_2) is commonly considered as an interesting efficient catalyst in photocatalytic treatments under UV radiation due to its affordable cost, its lack of toxicity and its environmentally friendly nature. The anatase phase is usually employed in most photocatalytic studies, although an optimized mixture of anatase and rutile as employed in the benchmark catalyst Degussa-25 usually shows higher catalytic activities [16]. Recent development of TiO_2 include the development of TiO_2 nanoparticles (<10 nm) for boosting the photocatalytic activity [17,18], as well as doping with transition metals (e.g., V, Cr, Mn, Fe, Co, Ni, Cu, W) [19,20], nitrogen [21–23], and carbon [24] to reduce the band gap energy promoting transitions to the visible spectral range.

The practical implementation of TiO_2 in photocatalytic applications requires the development of supports allowing a high dispersion of immobilized TiO_2 nanoparticles, a proper penetration of UV radiation to the active sites, and a high adsorption capacity of VOCs. Different materials have been tested as TiO_2 supports, including silica (e.g., glass, quartz, optical fibres [25], molecular sieves [26–28]), stainless steel [29,30], organic polymers [31], carbon fibres [32], activated carbon and alumina [33], and cotton fibres [34–36]. Comparative studies have been reported pointing out the crucial role of the support nature and TiO_2 formulation on the photocatalytic activity.

In addition to these supports, TiO_2 -loaded paper sheets have been proposed for air treatment applications. TiO_2 can be immobilized in paper fibres via two general approaches [37]: (1) *coating process*, where a titania suspension is coated on the sheet surface, and (2) *wet-end addition*, where titania nanoparticles are introduced into a cellulosic fibre suspension before sheet formation, leading to a bulk distribution of the TiO_2 loading. A binder can be used in the former approach to promote the loading and dispersion of the TiO_2 phase in the paper and to protect the fibres against radiation. Examples of TiO_2 -coated papers have been reported using silica [38–40], clinoptilolite [41,42], silicone [43], polydiallyldimethylammonium chloride [44,45], and aluminium hydroxide + polyamide/polyamine [46] binders. Silica binders usually provide TiO_2 -coated papers with higher activities in VOC degradation, approaching in some cases to the values achieved on finely dispersed TiO_2 [40]. However, the photocatalytic activity can be strongly inhibited by water poisoning due to competitive adsorption on the active sites [38].

The first demonstrative study on the manufacture of photocatalytic paper sheets was reported by Matsubara et al. [46] for the abatement of acetaldehyde under weak fluorescent light illumination. Later on, Tanaka and co-workers [44,47] prepared several types of photocatalytic paper composites with a dual polymeric retention system using TiO_2 supported on inorganic fibres. The papers were found effective for the removal of bisphenol in wastewater and acetaldehyde and toluene from indoor air. Bordiga et al. [35] reported the preparation of titania-supported photoactive cellulose fibres (3–5 nm anatase) using a sol–gel method at low temperature. The paper sheet showed optimal photocatalytic activity and stability when exposed to solar-like light for the degradation of methylbenzene blue and heptane-extracted bitumen fraction containing a mixture of heavy aromatic hydrocarbons. Finally, Raillard et al. [38] and Fukahori et al. [45] reported a kinetic study on the decomposition of different VOCs using titania-containing

papers, with special insight into the effect of the void structure of the papers on the degradation performance.

In this study, we present the preparation of a novel photocatalytic paper by wet-end addition consisting of sol–gel titania nanoparticles immobilized on porous silica as an attempt to promote both the photocatalytic activity by increasing TiO_2 accessibility by the UV radiation and the stability of the papers. The photocatalytic papers have been tested in the near-room temperature decomposition of ethanol vapour under an air carrier stream as model system.

2. Experimental

2.1. Materials

Calcium carbonate OMYA Hydrocarb 90 with a mean size of 700 nm was used as an inorganic template for silica synthesis. Sodium silicate (27 wt.% SiO_2 , 10 wt.% NaOH, Riedel de Haën), sodium hexametaphosphate (pure, Acros Organics) and hydrochloric acid (37 wt.%, Roth and Chimie Plus) were used in the synthesis of silica particles. Titanium tetra-isopropoxide (TTIP 98%) and 2-propanol, both supplied by Acros Organics, were used in the preparation of sol–gel derived TiO_2 colloids. Nitrogen (purity 99.995%) was supplied by Air Liquide. Bleached softwood Kraft pulp from Fibre Excellence Group (plant of Tarascon) was used for the preparation of photocatalytic paper. Cationic polyacrylamide (C-PAM, FENNOPOL K3400 R from KEMIRA Pulp and paper chemicals) was used as retention agent in the silica-based TiO_2 papermaking system. Non-woven photocatalytic paper was purchased from Ahlstrom, France (BR048-75, 60% synthetic fibres, 20% cellulosic fibres, 20% SiO_2 binder, 75 g m⁻² fibres basis weight, 18 g m⁻² TiO_2 basis weight).

2.2. Preparation of the silica binder

The protocol for the synthesis of silica particles was adapted from the patent literature [48–50]. Fig. 1 illustrates the synthetic approach. Briefly, CaCO_3 was dispersed in 1 L of water using an ultrasound probe (Branson Sonifier 250) with 1 wt.% sodium hexametaphosphate. Sodium silicate ($\text{Na}_2\text{Si}_3\text{O}_7$) diluted twice was added dropwise (2 h) into the CaCO_3 suspension kept at 80.0 °C using a thermostated water bath (LAUDA Ecoline staredition 003) and at pH=9 by adding a HCl solution (0.1 M). The suspension was filtered and rinsed with distilled water. The composite was then dispersed in 0.5 L water and the suspension was kept at pH=4 by adding a HCl solution (2 M) overnight at 80.0 °C to remove the CaCO_3 template. The resulting gel was filtered, rinsed again and calcined at 200 °C to obtain the porous silica particles.

2.3. Preparation of TiO_2 nanoparticles

The monodispersed TiO_2 nanoparticles were prepared by a sol–gel method using the standard procedure described elsewhere [51–54]. The sol–gel syntheses was conducted in a thermostated (20.0 °C) reactor with T-mixer, which puts in contact two fluids from a 50-mL stock solutions: (A) 0.292 M titanium tetraisopropoxide (TTIP) in 2-propanol and (B) 0.584 M distilled water

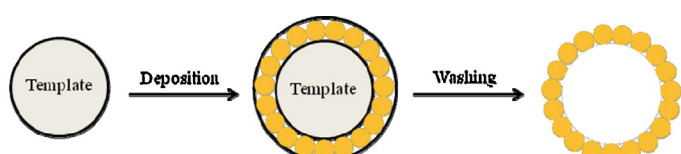


Fig. 1. Strategy for preparing the silica binder via CaCO_3 templating.

in 2-propanol. The flow rate in the main output tube of the T-mixer with Reynolds number of 4500 was maintained by applying an external dry N₂ gas pressure. The particle size is monitored in-situ using optical fiber probe by dynamical light scattering method.

Using this protocol, the nucleation proceeds rapidly ($t < 10$ ms) when the reagent passes through the T-mixer. The obtained titanium-oxo-alkoxy (TOA) nuclei with 5-nm hydrodynamic diameter are of non-crystalline nature: they consist of ~4 nm TiO₂ core and reactive hydroxyl and propoxy surface groups. These nanoparticles grow slowly in size during the induction period $t_{ind} = 55$ min, after which the colloid loses stability and the nanoparticles precipitate. The TOA nanoparticles can be easily immobilized during the period of a relative colloid stability: $t < t_{ind}/2$ [55]. In the present work, the silica support was immersed into the reactive solution for 10 min, then removed and dried at 80.0 °C. At contact, the TOA nanoparticles react with surface hydroxyls and tightly fixed on the support. Since the silica particles are porous, titania nanoparticles are expected to be transported by capillary forces, reacting both on the open surface of silica and in the pores of nearby silica grains. When necessary, the deposition process was repeated several times (up to three) on the same silica sample to increase the TiO₂ mass loading. After the deposition, the TOA-anchored silica was calcined at 450–800 °C under ambient air in order to induce the crystallization of anatase TiO₂ polymorph, which is the most active in photocatalysis.

2.4. Preparation of the photocatalytic paper

Paper sheets (diameter 20 cm) with various basis weights (60, 100 and 200 g m⁻²) were prepared according to the "Rapid Khoten" method following the ISO 5269-2 standard [56]. The pulp fibres were mechanically refined to approximately SR38 (Schopper Riegler degree) according to ISO 5264-1 [57] and ISO 5267-1 [58] standards prior to blending with the other materials. The titania-supported silica, calcined at different temperatures, was dispersed in 50 mL distilled water for 10 min using an ultrasound probe and then added to the pulp suspension under mild stirring followed by the addition of C-PAM as retention agent 0.1 wt.% of dry fiber. The titania-supported silica loading ranged from 10% to 40% of the total weight paper sheet. The paper sheets were formed on 200 mesh wires using a standard hand-sheet forming machine and dried under the standard conditions described by the TAPPI T402 test method [59]. The silica-titania retention was measured according to the TAPPI T211 method [60]. The basis weight of the as-obtained papers was measured using the ISO 536 standard [61].

2.5. Physical characterization

The titania loading in TiO₂/SiO₂ particles was measured by inductive coupled plasma analysis (ICP-AES) using a Spectroflame-ICP system. Before the measurements, the samples were dissolved using a H₂SO₄/HNO₃/HF solution at 423 K.

The specific surface area and pore volume of the silica particles were measured from N₂ adsorption-desorption isotherms at 77 K using a Micromeritics ASAP 2010 Surface Area Analyzer. The surface area was calculated by the Brunauer–Emmett–Teller (BET) method in the relative pressure range $0.05 < P/P_0 < 0.25$, while the pore size distribution was measured by the Barrer–Joyner–Halenda (BJH) method at $P/P_0 = 0.99$, and the microporous volume was estimated by the t-plot method. Prior to the measurements, the silica samples were degassed at 673 K under vacuum (10^{-2} Pa) during 4 h.

The phases present in TiO₂/SiO₂ composites were analysed by X-ray diffraction (XRD) and Raman spectroscopy. XRD analyses were carried out using a PANalytical X'Pert Pro Diffractometer provided with a Cu-K α radiation ($\lambda = 1.5418$ Å). Raman spectroscopy was

performed with a Renishaw In-via Raman spectrometer. Spectra were obtained with the green line of an Ar-ion laser (514.53 nm) operated in micro-Raman configuration (objective $\times 50$) at 8.2 mW.

The morphology and structures of the porous silica and titania-supported silica nanoparticles were inspected by high resolution transmission electron microscopy (HRTEM) (JEOL 2010 LaB₆, 20 kV) equipped with energy dispersive spectroscopic (EDX) microanalysis (LinK ISIS, Oxford Instruments) and electron diffraction (ED) analysis. The samples were immobilized on a resin and then cut to a thickness of 5 nm using a Leica Ultracut (UCT) ultramicrotome. The morphology of the paper sheets was inspected by Scanning Electron Microscopy (SEM) on a Quanta 200 microscope (10 kV) equipped with EDX analysis.

2.6. Textural properties of the papers

The thickness of the papers sheets, L (m), was measured using a MI 20 high-precision micrometer from ADAMEL LHOMARGY. For each paper, the measurements were carried out on at least 10 paper sheets with a maximum experimental error of 5%.

The permeability (air), B_0 (m²), of the papers was measured using the Darcy Law according to the NF Q03-076 standard on a BENDTSEN device [62]:

$$B_0 = \frac{\mu U L}{\Delta P} \quad (1)$$

where U is the superficial velocity of air measured by the BENDTSEN device (m s⁻¹), μ is the air viscosity (1.8×10^{-5} kg m⁻¹ s⁻¹ at 298 K [63]), and ΔP is the transpaper pressure difference (1.47 kPa). For each paper, the permeability measurements are given as the mean value of at least 10 measurements with a maximum experimental error of 5%.

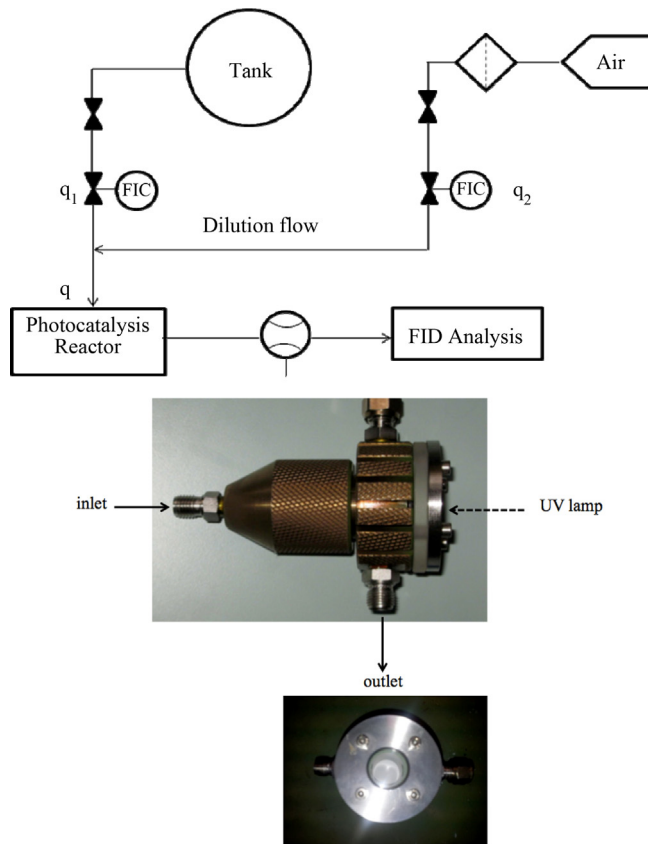


Fig. 2. Schematic representation of the setup used for measuring photocatalytic activities.

error of 5%. The permeability will be expressed in term of “Bendtsen permeability” mL(STP/min), corresponding to the air flow rate measured for a given pressure drop by the BENTDSEN device.

2.7. Aging tests

Some photocatalytic papers were subjected to a standard aging test to assess for the stability under UV irradiation. The aging tests were performed using a Xenotest 150 Cassalla system operating at 1500 W and surrounded by a filter system to simulate a part of the UV solar radiation ($\lambda = 360$ nm). Paper samples with a standard dimension of 4.5 cm \times 13 cm were placed in a sampler and introduced into the device. The samples were exposed to UV radiation for 18, 24, and 48 h. After the aging period, the degree of whiteness R457 was measured according to ISO 2470-1 [64].

2.8. Evaluation of the photocatalytic activity

The photocatalytic performance of the TiO₂/SiO₂ loaded papers was studied in a stainless-steel continuous gas-flow reactor (diameter, 22 mm; volume, 10 mL) using the setup schematically depicted in Fig. 2. Ethanol was chosen as model VOC pollutant at concentrations in the range 50–200 mg m⁻³ ($\pm 10\%$). Briefly, a tank (168 L) was equipped with a septum injection system and a manometer. Ethanol was injected with a syringe under primary vacuum ensuring its vaporisation. Then, the tank was fed with filtered and compressed air until the desired pressure (350 kPa). A second gas stream was used to dilute the concentrated effluent coming from the tank up to the desired ethanol concentration. The gas flow rate was measured using mass flow controllers (Bronkhorst, range 0–1000 mL(STP)/min).

The overall gas flowrate entering the reactor was about 500 mL(STP)/min in all the experiments, while the temperature was kept at 28 ± 3 °C using an external air flow. A UV lamp (HPK 125 W, Philips, emission band centred at 365 nm, radiation intensity of 12–14 mW m⁻²) was used as UV radiation source and placed in the same or opposite direction compared to the inlet air flow (i.e., co- and counter-current configuration modes). The incident UV intensity was measured using a VLX-3 W radiometer equipped with two sensors (254 and 365 nm) matching the diameter of the reactor. The ethanol concentration at the outlet of the reactor was monitored using a GC (Perkin Elmer 8500) equipped with an injection loop and a Flame Ionisation Detector (FID). The GC was equipped with a capillary column HP1 of 30 m length and 0.25 mm inner diameter. The papers were saturated in ethanol by the gas flow before

switching on the UV lamp to prevent adsorption kinetic effects on the measured photocatalytic activities.

The steady-state ethanol conversion, X_{EtOH} , was defined as the concentration difference between the reactor inlet (C_0) and outlet at steady-state values (C) compared to the inlet value, whereas the photocatalytic activity was defined as the converted ethanol flow-rate [$Q(C_0 - C)$], compared to the total TiO₂ mass loading on the paper (W_{TiO_2}), that is

$$X_{EtOH} = \frac{C_0 - C}{C_0} \quad (2)$$

$$\text{Activity} = \frac{Q(C_0 - C)}{W_{TiO_2}} \quad (3)$$

In the latter definition, it was implicitly assumed that the paper behaves as a continuous stirred-tank reactor under perfect mixture and that all deposited TiO₂ is active, which is not exactly true for our system due to the incomplete UV penetration into the paper layer. This issue will be addressed in the Discussion section.

3. Results and discussion

3.1. Characterization of the silica support

Fig. 3A shows a representative TEM micrograph of an as-synthesized hybrid silica–CaCO₃ particle after the deposition of silica on the CaCO₃ template particle, confirming the prevalence of the heterogeneous primary nucleation mechanism and further growth in the genesis of the silica particles. Fig. 3B shows the final morphology of the silica particles generated after acidification, revealing the formation of an open silica structure after CaCO₃ removal.). The particles show a specific surface of about 102 m² g⁻¹, a total pore volume of 0.32 cm³ g⁻¹ (<0.01 cm³ g⁻¹ microporous), and a broad pore size distribution in the range 10–80 nm centered at 24 nm, as inferred from N₂ adsorption/desorption at 77.4 K. This pore size is larger than the mean size of the titania nanoparticles to be further immobilized (3–10 nm), making this support suitable for the preparation of the TiO₂/SiO₂ composites for photocatalytic applications.

3.2. Characterization of the TiO₂/SiO₂ particles

Elementary analyses confirm the increasing TiO₂ loading on the silica particles as a function the number of deposits. Fig. 4A shows the XRD patterns of the as-synthesized TiO₂/SiO₂ particles

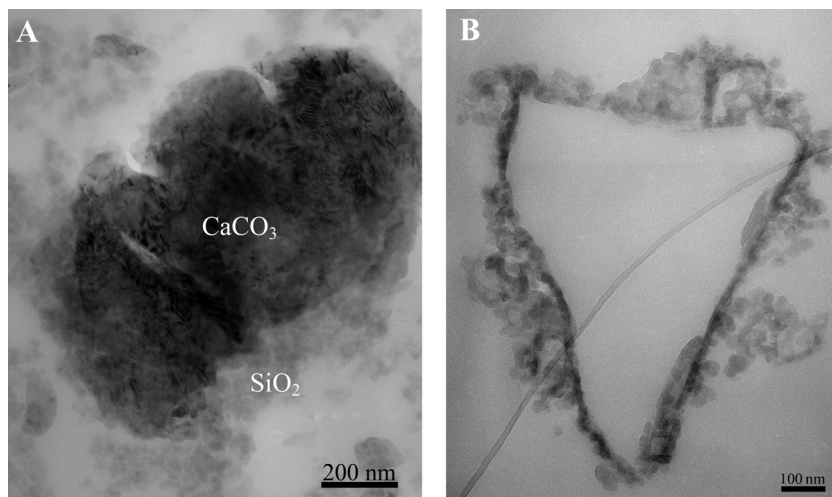


Fig. 3. (A) TEM micrograph of a CaCO₃–SiO₂ hybrid particle (B) TEM micrograph of a silica particle after CaCO₃ removal by acidification.

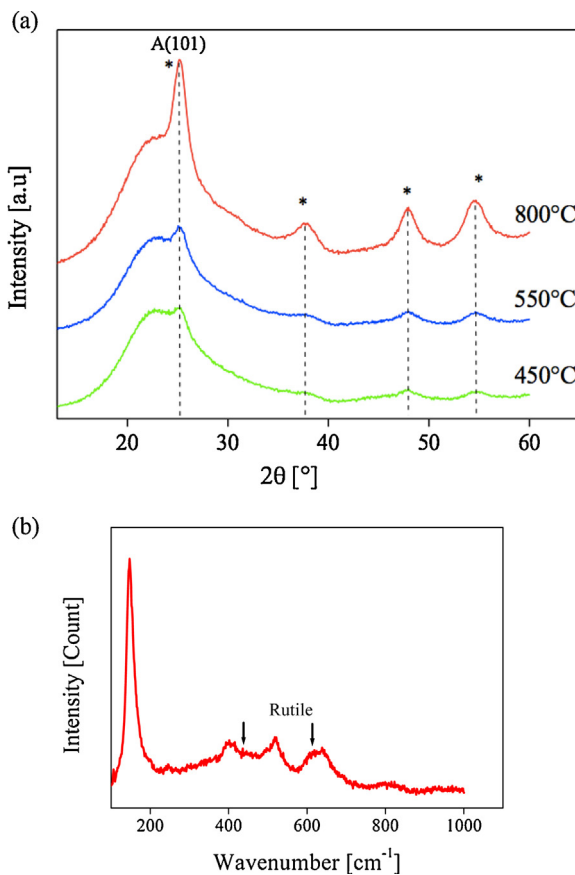


Fig. 4. (A) XRD patterns of the composite $3\text{TiO}_2/\text{SiO}_2$ catalyst subjected to different calcination temperatures and (B) Raman spectra (bottom) of the same catalyst after calcination at 800°C .

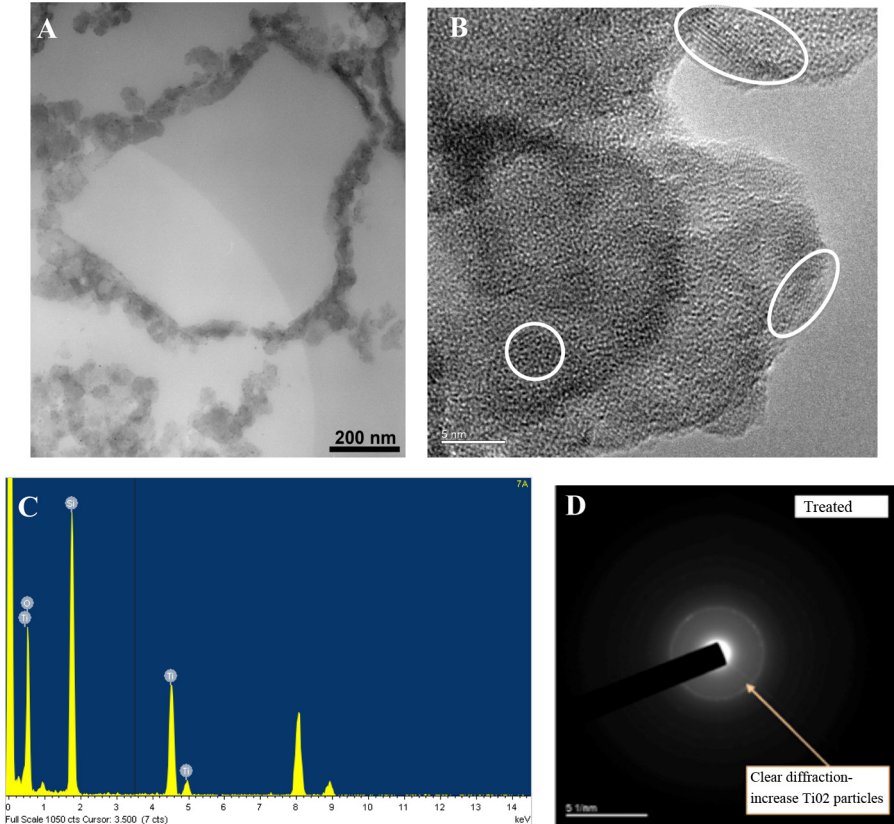


Fig. 5. (A) TEM micrograph of $3\text{TiO}_2/\text{SiO}_2$ particles after crystallization at 800°C , (B) TEM micrograph pointing out the local distribution of TiO_2 nanoparticles, (C) EDX and (D) ED analyses of $3\text{TiO}_2/\text{SiO}_2$ particles after crystallization at 800°C .

at different calcination temperatures ranging from 450 to 800°C . The amorphous phase belonging to silica is maintained at all temperatures. The TiO_2 anatase phase is obtained at the different calcination temperatures without evidence of an anatase-to-rutile phase transition even after heating at 800°C . Titania crystallization is apparently completed beyond 800°C . Such observation is consistent with the Raman spectra obtained for the sample calcined at 800°C (Fig. 4B), showing characteristic bands centred at 143 , 196 , 396 , 515 and 639 cm^{-1} belonging to vibration modes of anatase. However, the presence of rutile impurities cannot be ruled out, as inferred from the subtle bands around 450 and 610 cm^{-1} .

The unexpectedly high crystallization temperature of our silica-supported titania nanoparticles contrasts with the conventional crystallization temperature reported for anatase, being about 450°C [65]. The observed in the present study abnormally high crystallization temperature in high-purity silica-covered large specific area alumina supports has been recently reported by Bouslama et al. [66,67]. This can be explained by a small size (below the critical one of $\sim 15\text{ nm}$) and weak interaction between single (non-agglomerated) TiO_2 nanoparticles. The same group of authors has also shown that the amorphous-anatase phase transformation process is delayed up to 500°C in this system and the complete anatase crystallisation is achieved at 800°C [68]. The last work supports the present observation of the photocatalytic activity of the prepared materials discussed in Section 3.4.

The sample calcined at 800°C was additionally inspected by TEM, EDX and ED in order to visualize the nature and dispersion of the immobilized TiO_2 nanoparticles on the silica support (Fig. 5). The TEM micrographs confirm the genesis of small nanoparticles with a size below 10 nm dispersed on the silica support in agreement with the XRD patterns and Raman spectra. Macroscopically, the particles show no preferential orientation, as deduced from

the relatively continuous cycles in the ED analyses. However, the individual orientation of a single nanoparticle to the support may be pre-defined by the interface. The EDX analyses confirm the presence of TiO_2 on the silica particles by the presence of a characteristic peak at about 4.5 keV. The peaks show an increasing value with the TiO_2 loading (not shown) as a function of the number of sol-gel deposition cycles. No peak corresponding to Ca was observed in the EDX spectra, suggesting the absence of trapped Ca in the $\text{TiO}_2/\text{SiO}_2$ particles. This result supports the formation of stable Ti–O–Si bond at the interface between TiO_2 and SiO_2 as the underlying reason for the high crystallization temperatures required for our anatase formation in our $\text{TiO}_2/\text{SiO}_2$ samples.

The specific surface of the $\text{TiO}_2/\text{SiO}_2$ samples was found to increase inversely with the crystallization temperature compared to the parent silica support for the same number of TiO_2 deposits. This result can be explained on the basis of a partial yet moderate sintering of titania nanoparticles. The specific surface of the $\text{TiO}_2/\text{SiO}_2$ sample treated at 800 °C shows a decrease about 20% after treatment from an initial value of $152 \text{ m}^2 \text{ g}^{-1}$. Noteworthy, this specific surface is comparable to the standard values of TiO_2 after calcination at 400–500 °C [69], and comparatively higher than the specific surface of commercial Degussa P25 titania (about $60 \text{ m}^2 \text{ g}^{-1}$).

Furthermore, the weight fraction of the TiO_2 phase in the $\text{TiO}_2/\text{SiO}_2$ particles can be estimated by Eq. (3) if we assume that the specific surface of the composite particles can be divided into two additive contributions corresponding to the TiO_2 and SiO_2 phases.

$$x_{\text{TiO}_2} = \frac{S_g(\text{TiO}_2/\text{SiO}_2) - S_g(\text{SiO}_2)}{S_g(\text{TiO}_2) - S_g(\text{SiO}_2)} \quad (3)$$

In Eq. (3), a value of $350 \text{ m}^2 \text{ g}^{-1}$ was used for TiO_2 nanoparticles assuming a spherical shape with a mean oxide core size of 4.4 nm [54] and a density of 3.89 g cm^{-3} (anatase), whereas a value of $102 \text{ m}^2 \text{ g}^{-1}$ was used for the bare silica support. The application of Eq. (3) to the $\text{TiO}_2/\text{SiO}_2$ particles obtained after 3 titania deposits reflects a weight fraction about 13.8 wt.%, which is consistent with the value of 13.2 wt.% measured by direct weight uptake after the third deposit (*vide supra*).

3.3. Manufacture of silica-titania paper sheet

The particle size distribution of the $\text{TiO}_2/\text{SiO}_2$ composites was measured before introduction into the fiber suspension using particle size analyser type 1190. The results show a bimodal distribution centred at 0.2 and 3.0 μm (Fig. 6) mainly attributed to the silica support.

A preliminary study on a paper sheet with 80 g m^{-2} basis weight was carried out to assess the effect of C-PAM and basis weight on the $\text{TiO}_2/\text{SiO}_2$ load retention in the paper. The retention was found

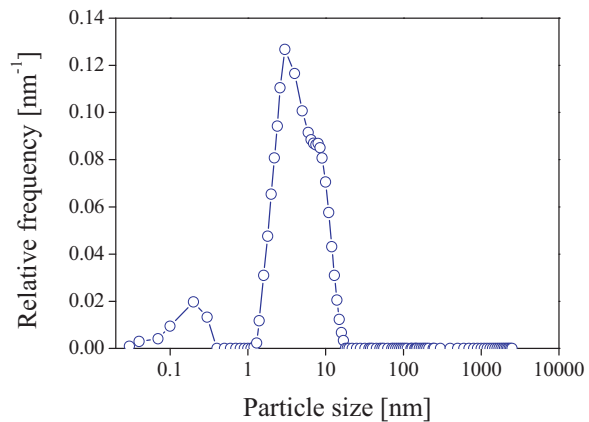


Fig. 6. Particle size distribution of $\text{TiO}_2/\text{SiO}_2$ composites.

to increase from 8% in the absence of C-PAM to a maximum value of 82% for a C-PAM concentration of 0.1 wt.% corresponding to the standard value reported in the literature [70]. The retention also increased slightly with the basis weight of the paper. This observation can be explained by the relatively high Schopper-Riegler degree of the papers (about SR 38), facilitating further compactness during manufacture. Table 1 summarizes the main characteristics of the different papers prepared in this study with variable basis weights and TiO_2 loadings.

Figs. 7 and 8 show, respectively, the top view and cross section SEM images of a representative $\text{TiO}_2/\text{SiO}_2$ loaded paper sheet with 200 g m^{-2} basis weight. The paper shows a well fibrillated texture with well-dispersed $\text{TiO}_2/\text{SiO}_2$ particles on the paper surface and within the thickness, but forming some spherical-shaped agglomerates (about 90 μm) that do not appear to block the paper voids, facilitating gas passage during the further photocatalytic tests.

The main composition and distribution of the main elements of the above stated $\text{TiO}_2/\text{SiO}_2$ -loaded paper sheet was inspected by EDX mapping (Fig. 7B–D). As expected, C atoms are distributed onto the paper according to the position of the fibres (Fig. 7A,B). The Ti and Si atoms are homogeneously distributed out of these fibres, suggesting an optimal incorporation of the $\text{TiO}_2/\text{SiO}_2$ catalyst. The Ca mapping (not shown) indicates the presence of an extremely low (but not negligible) amount of Ca atoms well dispersed within the sample. We attribute this broad distribution to Ca arising from water hardness instead of CaCO_3 template residues after silica preparation. Indeed, in the latter case, Ca atoms would be expected to be preferentially localized near the silica positions, which is not the case observed here.

The cross section of the paper sheets (Fig. 8) is constituted by several layers of fibres intercalated by the $\text{TiO}_2/\text{SiO}_2$ charge. The basis weight and $\text{TiO}_2/\text{SiO}_2$ loading exerts an important effect

Table 1

Main characteristics of the different papers prepared in this study.

| Paper | Basis weight (g/m ²) | Catalyst used, calcination temperature* | $\text{TiO}_2/\text{SiO}_2$ loading (wt.%) | TiO_2 loading (wt.%) | TiO_2 basis weight (g/m ²) | Thickness (μm) | Bendtsen permeability (mL(STP)/min) | Degradation amount [$\text{-} \times 100^{**}$] |
|-------|-------------------------------------|---|---|----------------------------------|--|-----------------------------|---|--|
| P1 | 200 | 1 $\text{TiO}_2/\text{SiO}_2$, 800 °C | 40 | 1.7 | 3.3 | 466 ± 8 | 340 ± 3 | 26.8 |
| P2 | 200 | 2 $\text{TiO}_2/\text{SiO}_2$, 800 °C | 40 | 3.4 | 6.9 | 477 ± 9 | 333 ± 6 | 37.1 |
| P3 | 200 | 3 $\text{TiO}_2/\text{SiO}_2$, 800 °C | 40 | 4.8 | 9.6 | 421 ± 6 | 330 ± 2 | 47 |
| P4 | 200 | 1 $\text{TiO}_2/\text{SiO}_2$, 450 °C | 40 | 1.7 | 6.9 | 535 ± 2 | 322 ± 7 | 19 |
| P5 | 200 | 2 $\text{TiO}_2/\text{SiO}_2$, 450 °C | 40 | 3.4 | 3.3 | 438 ± 6 | 320 ± 5 | 23.6 |
| P6 | 200 | 3 $\text{TiO}_2/\text{SiO}_2$, 450 °C | 40 | 4.8 | 9.6 | 456 ± 3 | 326 ± 3 | 29.5 |
| P7 | 100 | 3 $\text{TiO}_2/\text{SiO}_2$, 800 °C | 10 | 1.3 | 1.3 | 189 ± 5 | 1873 ± 2 | 21 |
| P8 | 100 | 3 $\text{TiO}_2/\text{SiO}_2$, 800 °C | 40 | 4.5 | 4.5 | 209 ± 7 | 814 ± 4 | 27 |
| P9 | 60 | 3 $\text{TiO}_2/\text{SiO}_2$, 800 °C | 12.5 | 0.9 | 1.6 | 139 ± 4 | 1384 ± 1 | 22 |

*The number 1, 2 or 3 refers to the number of deposit.

**Experimental conditions: $C_0 = 50 \text{ mg/m}^3$, flow rate: 500 mL(STP)/min, incident UV radiation = 14.4 mW/cm², counter-current mode.

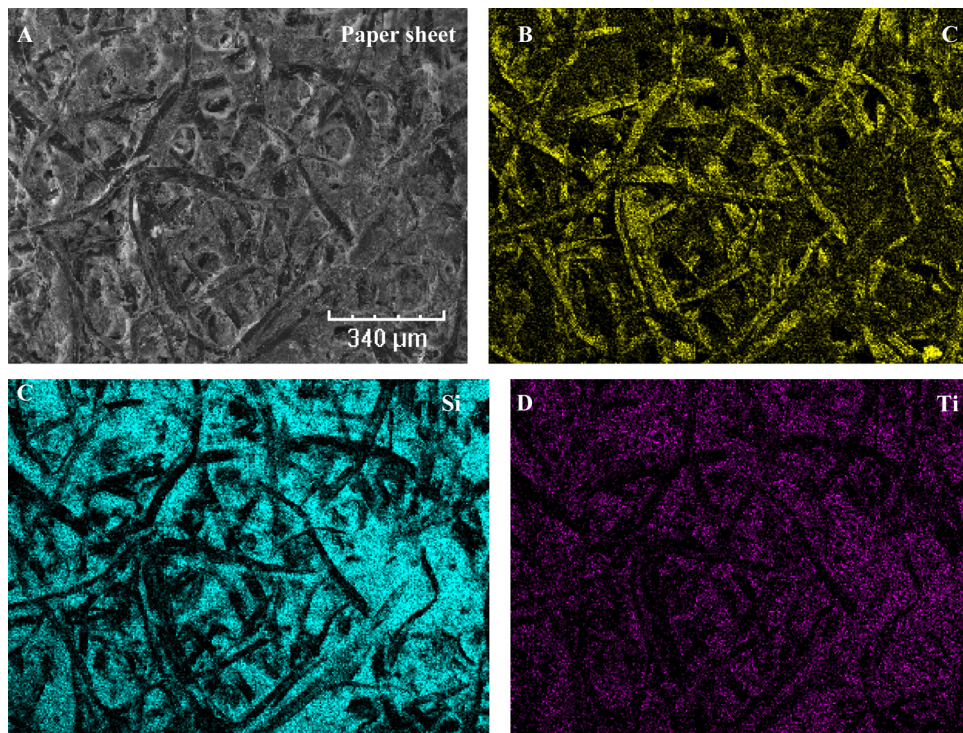


Fig. 7. A) Top view SEM micrograph of paper sheet P3 with 200 g m^{-2} basis weight and 40 wt.% $\text{TiO}_2/\text{SiO}_2$ loading, and corresponding EDX cartography of (B) carbon, (C) silicon and D) titanium elements.

on the paper thickness and densification, allowing a facile tuning of the textural properties of the papers. For instance, for a basis weight of 100 g m^{-2} , the air permeability decreases from 1873 to $814 \text{ mL(STP)} \text{ min}^{-1}$ with an increase of the $\text{TiO}_2/\text{SiO}_2$ loading from 10 to 40 wt.% (Table 1), papers P7 and P8). Besides, for $\text{TiO}_2/\text{SiO}_2$ loading of 40 wt.%, an increase of the basis weight from 100 to 200 g m^{-2} leads to a decline of the air permeability from 814 to $330 \text{ mL(STP)} / \text{min}$ (Table 1, papers P8 and P3).

3.4. Photocatalytic activity of photocatalytic paper

3.4.1. Preliminary tests

Photocatalytic tests were performed on all the samples shown in Table 1, in which the degradation amount is given for specific running condition. In the following section, only papers with the best activity (P3 and P6) were discussed. The photocatalytic performance of the $\text{TiO}_2/\text{SiO}_2$ -loaded papers in the degradation of ethanol was first inspected as a function of the titania calcination temperature.

Fig. 9 shows the photocatalytic decomposition kinetics of papers P3 and P6 with the same basis weight (200 g m^{-2}), $\text{TiO}_2/\text{SiO}_2$ loading (40 wt.%), and TiO_2 loading (4.8 wt.%), but subjected to TiO_2 crystallization temperatures of 800 and 450°C , respectively. For comparison, the corresponding curve for a base paper with no TiO_2 is also plotted. An important result is that the ethanol decomposition is faster in paper P3, containing TiO_2 calcined at 800°C , compared to P6, where TiO_2 is expected to be not completely converted to anatase [68].

In a second step, a series of photocatalytic tests were carried out to assess the influence of the basis weight and air permeability on the photocatalytic activity of the *as-prepared* papers. To this aim, we tested three papers with variable basis weights (60, 100 and 200 g m^{-2} , respectively, Table 1, papers P9, P7 and P1) and low TiO_2 loadings (0.9, 1.3 and 1.7 wt.%, respectively) on TiO_2 calcined at 800°C . Note that the former two basis weights and the TiO_2

loading are comparable to the values used by Ko et al. [41,42] and Matsubara et al. [46], respectively on TiO_2 -loaded and TiO_2 -coated papers. In all cases, the ethanol conversion was found to not depend on the papers permeability, but on the TiO_2 mass loading. Our results oppose to the results reported by Fukahori et al. [45] in TiO_2 -coated papers, the porosity exerting a positive effect on the photocatalytic activity. Accordingly, we concentrated hereinafter our attention on papers with 200 g m^{-2} basis weight and a $\text{TiO}_2/\text{SiO}_2$ loading of 40 wt.% (Table 1) for promoting the photocatalytic activity.

Finally, we conducted specific tests (not shown) to assess the influence of the TiO_2 loading on the photocatalytic activity of the papers. As expected, the papers showing the richest TiO_2 content have the highest ethanol conversion, reaching a value as high as 47%. Further tests to assess the homogeneity

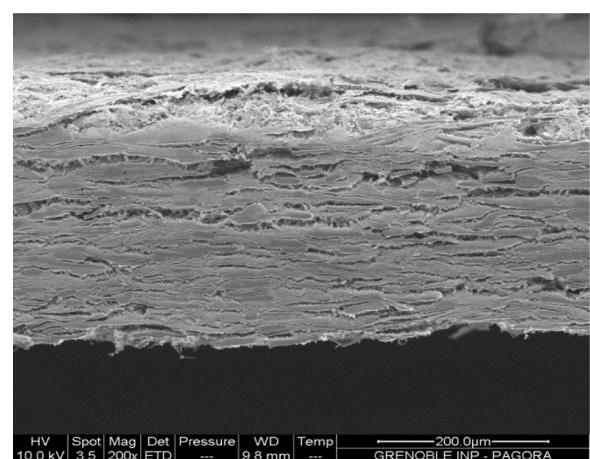


Fig. 8. Cross-section SEM micrograph of paper sheet P3 with 200 g m^{-2} basis weight and 40 wt.% $\text{TiO}_2/\text{SiO}_2$ loading.

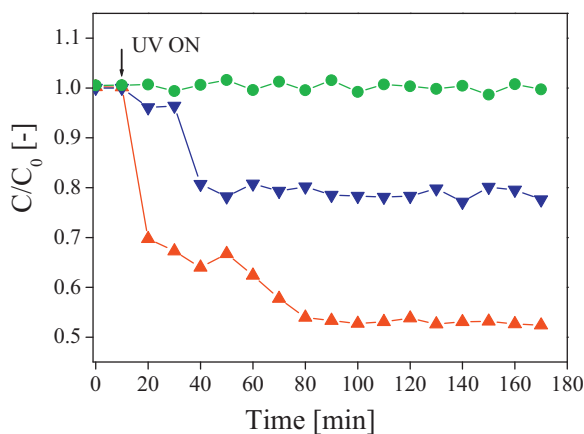


Fig. 9. Time evolution of the ethanol concentration for papers P3 (\blacktriangle) and P6 (\blacktriangledown) with different TiO_2 temperature (800 and 450 $^{\circ}\text{C}$, respectively), and basis weight of 200 g/m^2 , using 3 $\text{TiO}_2/\text{SiO}_2$ catalyst, $\text{TiO}_2/\text{SiO}_2$ loading of 40 wt.%, and TiO_2 loading of 4.8 wt.%. For comparison, the time evolution for a base paper with no TiO_2 is also represented (\bullet). Experimental conditions: inlet ethanol concentration, 50 mg/m^3 , air flow rate, 500 $\text{mL}(\text{STP})/\text{min}$; incident UV radiation, 14.4 mW cm^{-2} ; counter-current mode.

of the photocatalytic activity with the surface have been run by testing the photocatalytic activity of different slices cut from the same original paper and by irradiating both surfaces. As can be deduced from these tests, the $\text{TiO}_2/\text{SiO}_2$ charge shows a reasonable homogeneity in the photocatalytic activity, suggesting a fine dispersion within the paper thickness and at both surfaces.

3.4.2. Influence of the operational variables

Given the results presented above, we evaluate the influence of the main operation variables (i.e., inlet ethanol concentration, air flow rate, incident UV intensity and configuration mode) on the photocatalytic activity of paper P3. Figs. 10–12 collect the main trends obtained.

The inlet ethanol concentration (counter-current mode) exerts a pronounced effect on the ethanol conversion (Fig. 10), decreasing from 46% at 50 mg m^{-3} to 17% at 200 mg m^{-3} at a constant flowrate of 500 $\text{mL}(\text{STP})\text{ min}^{-1}$ and for an incident UV intensity of 14.4 mW cm^{-2} . However, the photocatalytic activity was enhanced from 3.85 $\text{mg g}_{\text{TiO}_2}^{-1} \text{ min}^{-1}$ at 50 mg m^{-3} to 4.71 $\text{mg g}_{\text{TiO}_2}^{-1} \text{ min}^{-1}$ at 200 mg m^{-3} [see Eq. (3)], as expected for a system driven by Langmuir-Hinshelwood kinetics without relevant blockage of TiO_2 active sites by intermediates (e.g., acetaldehyde). We conducted additional experiments to survey the effect of the air flow rate (or

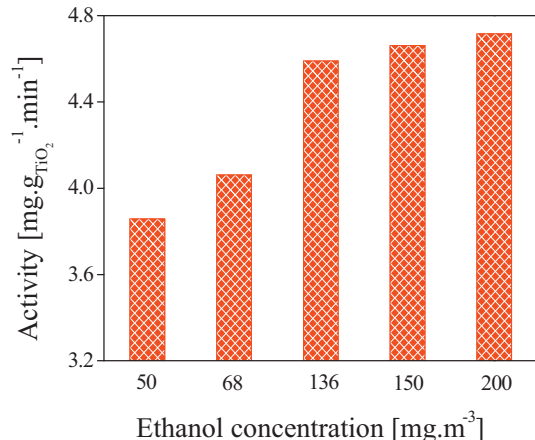
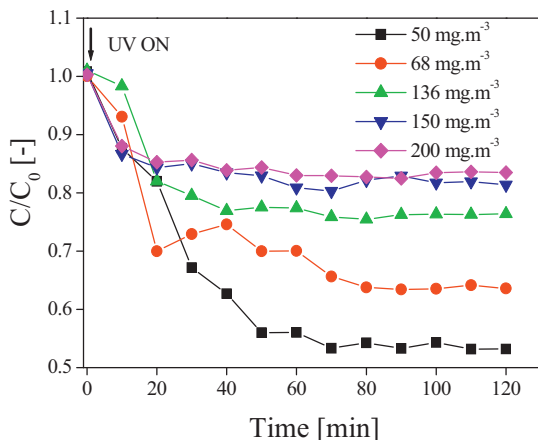


Fig. 10. Influence of the inlet ethanol concentration on the time evolution of ethanol degradation (A) and photocatalytic activity (B) of paper P3. Experimental conditions: inlet ethanol concentration: 50 mg/m^3 , air flow rate: 500 $\text{mL}(\text{STP})/\text{min}$; incident UV radiation: 14.4 mW cm^{-2} ; counter-current mode.

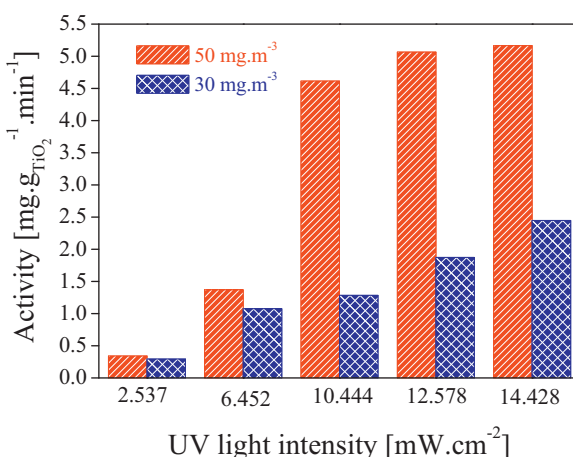
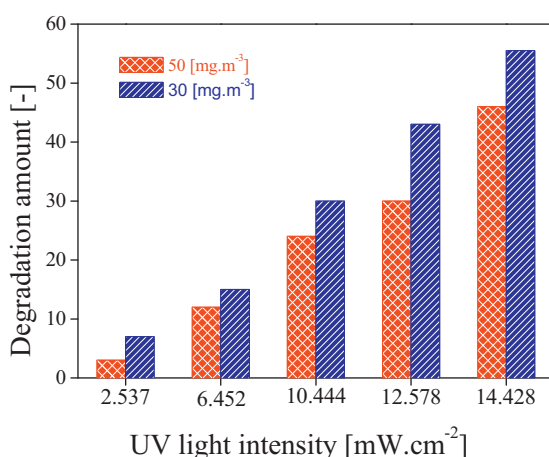


Fig. 11. Influence of the incident UV radiation on the ethanol degradation (A) and photocatalytic activity (B) of paper P3. Experimental conditions: inlet ethanol concentration: 30 and 50 mg/m^3 , air flow rate: 500 $\text{mL}(\text{STP})/\text{min}$; counter-current mode.

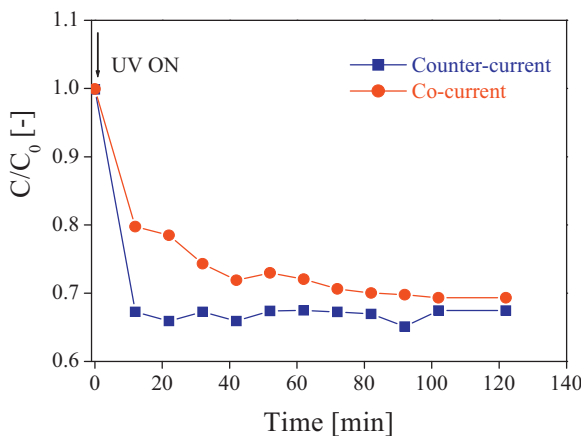


Fig. 12. Influence of the configuration mode on the ethanol concentration for paper P3. Experimental conditions: inlet ethanol concentration: 68 mg m^{-3} ; air flow rate: $500 \text{ mL(STP)} \text{ min}^{-1}$; incident UV radiation: 14.4 mW cm^{-2} .

superficial velocity) on the photocatalytic performance of paper P3 (not shown). Complete ethanol conversion was found for an air flow rate of $50 \text{ mL(STP)} \text{ min}^{-1}$ (13.2 cm min^{-1} or 0.2 s residence time) when operating with an inlet ethanol concentration of 68 mg m^{-3} and an incident UV intensity of 14.4 mW cm^{-2} in counter-current mode, corresponding to a photocatalytic activity of $0.93 \text{ mg g}_{\text{TiO}_2}^{-1} \text{ min}^{-1}$.

The incident UV intensity was found to exert a crucial effect on the ethanol conversion in paper P3 (Fig. 11), linearly increasing to 60% at 14.4 mW cm^{-2} in counter-current mode for an air flow-rate of $500 \text{ mL(STP)}/\text{min}$ and an inlet ethanol concentration of 30 mg m^{-3} . In terms of photocatalytic activities, the highest values are observed at higher inlet ethanol concentrations, reaching a value ca. $5.0 \text{ mg g}_{\text{TiO}_2}^{-1} \text{ min}^{-1}$ at 50 mg cm^{-3} and 14.4 mW cm^{-2} . Note that a UV intensity higher than 10 mW cm^{-2} is relevant for photocatalytic applications, since it approaches the value commonly achieved with solar light after deconvolution of the wavelength spectrum.

Finally, we carried out necessary tests to assess the influence of the operational mode (i.e., counter- and co-current) on the photocatalytic activity of paper P3 for an air flow rate of $500 \text{ mL(STP)} \text{ min}^{-1}$, an inlet ethanol concentration of 68 mg m^{-3} and an incident UV intensity of 14.4 mW cm^{-2} (Fig. 12). Within the limits of the experimental error, both configurations offer similar steady-state conversions (and activities). However, the counter-current mode presents a faster degradation rate (slope of the curve) near the paper inlet, most likely due to a deeper UV penetration within the paper thickness, providing higher concentration gradients. These observations suggest an important role of the axial diffusion within the paper thickness on mass transfer.

3.4.3. Stability tests

In order to evaluate a possible deactivation of photocatalytic papers, two consecutive degradation tests were performed on paper sheet P3 for an air flow rate of $500 \text{ mL(STP)} \text{ min}^{-1}$, an inlet ethanol concentration of 68 mg m^{-3} and an incident UV intensity of 14.4 mW cm^{-2} (Fig. 13). After the first test, the ethanol conversion reached a value of 47%. Subsequently, the lamp was tuned off, leading to an increase of the ethanol concentration to the inlet value. As soon as the concentration was stabilized, we performed a second degradation cycle by turning on again the UV lamp. The ethanol conversion was found to decrease by $\sim 15\%$ suggesting only a moderate deactivation of the TiO_2 phase during the dark period, which is probably due to acetaldehyde adsorption, as this has been

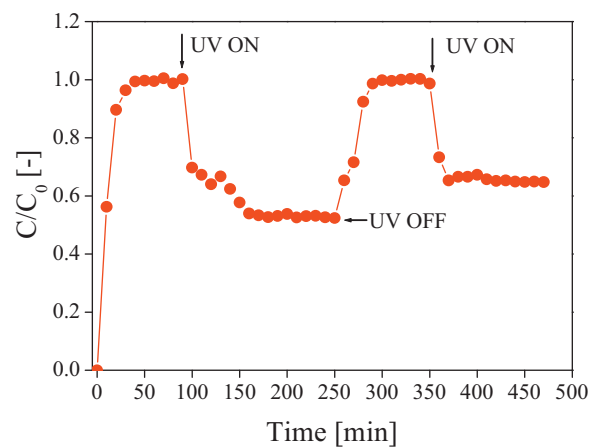


Fig. 13. Ethanol degradation in two consecutive degradation cycles for paper P3. Experimental conditions: inlet ethanol concentration: 50 mg m^{-3} ; air flow rate: $500 \text{ mL(STP)} \text{ min}^{-1}$; incident UV radiation: 14.4 mW cm^{-2} .

proposed in devoted studies on ethanol degradation [14,71]. However, partial deactivation by a degradation product of the fibres upon UV radiation cannot be excluded (*vide infra*). Notwithstanding this observation, the same sample recovered completely its activity after 2-day exposure to ambient air. This observation, in good keeping with former studies on TiO_2 -coated paper [71], can be explained by the total desorption of the adsorbed intermediate, consequently liberating the active sites.

Finally, we carried out aging tests of paper P3 by direct exposition of a representative sheet to a strong UV intensity (ca. 400 W.cm^{-2}) using a Xenotest 150 Casalla system at variable times (18–48 h) for an air flow rate of $500 \text{ mL(STP)} \text{ min}^{-1}$ and an inlet ethanol concentration of 50 mg m^{-3} . These tests provide relevant information on the life cycle of the papers subjected to strong UV radiation. The tested paper sheet showed a decline of the ethanol conversion from an initial value of 49% to 21%, corresponding to a change of the photocatalytic activity from $3.86 \text{ mg g}_{\text{TiO}_2}^{-1} \text{ min}^{-1}$ to $1.68 \text{ mg g}_{\text{TiO}_2}^{-1} \text{ min}^{-1}$ after 48 h. The degree of whiteness R457 of the paper sheet only decreases from an initial value of 88.0% to 83.4% after UV irradiation at 18–24 h. However, after treatment at 48 h, the paper sheet shows a slight yellow colour, involving a decrease of the degree of whiteness R457 down to 79.8%. This decrease of the degree of whiteness can be explained by the UV-assisted generation of free radicals on TiO_2 active sites, breaking covalent chains between the fibres and it seems to turn weakening the sheet. Consequently, the decrease of the photocatalytic activity after 48-h exposure to UV radiation can be explained by a poisoning of TiO_2 photocatalytic sites by molecules issued from the degradation of cellulose compounds. However, this poisoning is probably reversible.

3.4.4. Comparison with commercial benchmark paper

To assess for the competitiveness of our papers, we carried out a comparative study of paper P3 with a benchmark TiO_2 -coated paper supplied by Ahlstrom (BR048-75, 18 wt.% TiO_2 loading) for ethanol degradation. Fig. 14 plots the results obtained operating at the same conditions (air flow rate, $500 \text{ mL(STP)} \text{ min}^{-1}$; inlet ethanol concentration, 50 mg m^{-3} ; incident UV intensity, 14.4 mW cm^{-2} , counter-current mode). The ethanol degradation was found to be comparatively higher for the benchmark, showing a steady-state ethanol conversion about 75% compared to the value of 47% for paper P3. However, when computing the intrinsic photocatalytic activity (weighted to the deposited TiO_2 mass), paper P3 shows comparable values (ca. $5.0 \text{ mg g}_{\text{TiO}_2}^{-1} \text{ min}^{-1}$) at the above stated operation conditions. We notice that a lower TiO_2 loading 9.6 g m^{-2}

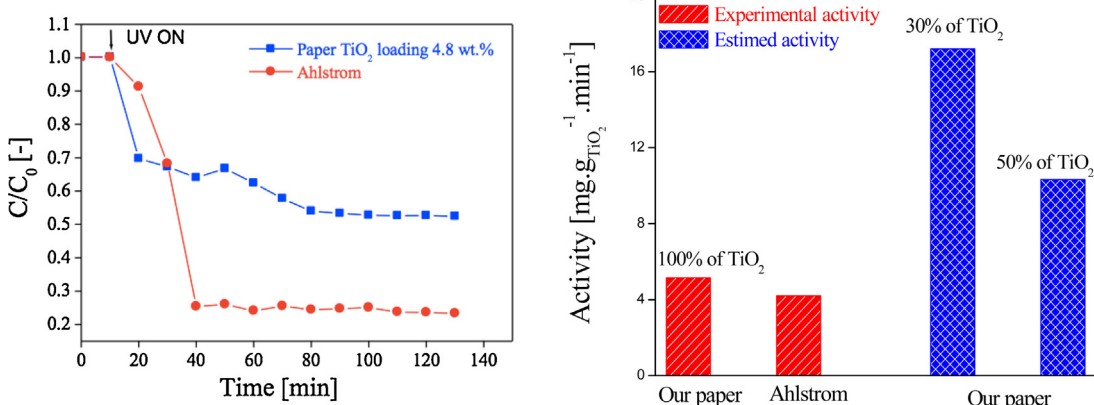


Fig. 14. Time evolution concentration of ethanol (A) and photocatalytic activity (B) for TiO₂-loaded paper P3 prepared in this study compared to the benchmark TiO₂-coated paper Ahlstrom BR 1048-075. For comparison, image B also plots the estimated activities considering different percentage of TiO₂ irradiated in the paper thickness. Experimental conditions: inlet ethanol concentration: 50 mg m⁻³; air flow rate: 500 mL(STP) min⁻¹; incident UV radiation: 14.4 mW cm⁻².

takes place in paper P3 compared to that of 18 g m⁻² in the benchmark.

Moreover, if we consider that only a small amount of the TiO₂ charge is conveniently irradiated by UV due to partial adsorption and scattering within the paper thickness, the effective activity of paper P3 appears to be higher. As an example, Fig. 14 plots the simulated photocatalytic activities assuming an optimal UV irradiation of 30% and 50% of the TiO₂ loading, leading to even more competitive photocatalytic activities compared to the benchmark paper. A convenient modelling of the UV profile within the paper sheets in our TiO₂-loaded papers appears to be crucial not only for a proper quantification of the irradiated TiO₂, but also for further optimization studies.

4. Conclusions

Nanosized sol-gel TiO₂/SiO₂-loaded photocatalytic paper composites have been successfully prepared using a retention papermaking system. The porous silica particles have been synthesized via CaCO₃ templating. The supported TiO₂ nanoparticles show an abnormally high amorphous-to-anatase crystallization temperature about 800 °C explained by small size and weak mutual interaction of supported titania domains, which confirm single nanoparticle nature of the realized depots.

The optimal photocatalytic performance of the silica-titania paper sheet has been demonstrated in the room-temperature degradation of ethanol, reaching a competitive activity as high as 3.86 mg g⁻¹ TiO₂ min⁻¹ for an incident intensity of 14.4 mW cm⁻². Further optimization studies are in progress to rationalize the UV intensity and concentration profiles within the paper sheets. The main conclusions of this study will be communicated in due time in a forthcoming publication.

References

- Council Directive 1999/13/CE of 11th March 1999 on the limitation of emissions of volatile organic compounds due to the use of organic solvents in certain activities and installations.
- Directive 2004/42/CE of the European Parliament and the Council of 21st April 2004 on the limitation of emissions of volatile organic compounds due to the use of organic solvents in certain paints and varnishes refinishing products and amending Directive 1999/13/EC.
- J.-P. Chang, J.-P. Fontelle, L. Serveau, Inventaire des émissions de polluants atmosphériques et de gaz à effet de serre en France: Séries sectorielles et analyses attendues (format Secten), CITEPA (ref. 880), Ministère de l'Ecologie, du Développement Durable, des Transports et du Logement, April 2011.
- R. Atkinson, *Atmosph. Environ.* 34 (2000) 2063–2101.
- J.A. Bernstein, N. Alexis, H. Bacchus, I.L. Bernstein, P. Fritz, E. Horner, N. Li, S. Mason, et al., *J. Allergy Clin. Immunol.* 121 (2008) 585–591.
- S.B. Wang, H.M. Ang, M.O. Tade, *Environ. Int.* 33 (2007) 694–705.
- EPA—An Introduction to Indoor Air Quality Pollutants and Sources of Indoor Air Pollution Volatile Organic Compounds (VOCs), available at <http://www.epa.gov/iaq/voc.html>, revisited 08/04/2013.
- M.A. Kolade, A. Kogelbauer, E. Alpay, *Chem. Eng. Sci.* 64 (2011) 1167–1177.
- S. Mudliar, B. Giri, K. Padoley, D. Satpute, R. Dixit, P. Bhatt, R. Pandey, A. Juwarkar, A. Vaidya, *J. Environ. Manag.* 91 (2010) 1039–1054.
- P. Le Cloirec, *Les composés organiques volatils (COV) dans l'environnement*, Tec&Doc Lavoisier, Paris, 1998, pp. 734.
- H.L. Chen, H.M. Lee, S.H. Chen, M.B. Chang, S.J. Yu, S.N. Li, *Environ. Sci. Technol.* 43 (2009) 2216–2227.
- L.F. Liotta, *Appl. Catal. B* 100 (2010) 403–412.
- W.B. Li, J.X. Wang, H. Gong, *Catal. Today* 148 (2009) 81–87.
- R.M. Alberici, W.F. Jardim, *Applied Catal. B* 14 (1997) 55–68.
- K. Demeester, J. Dewulf, H. van Langenhove, *Crit. Rev. Env. Sci. Technol.* 37 (2007) 489–538.
- R. Su, R. Bechstein, L. Sø, R.T. Vang, M. Silllassen, B. Esbjørnsson, A. Palmqvist, F. Besenbacher, *J. Phys. Chem. C* 115 (2011) 24287–24292.
- N. Xu, Z. Shi, Y. Fan, J. Dong, J. Shi, M.Z-C. Hu, *Ind. Eng. Chem. Res.* 38 (1999) 373–379.
- A.J. Maira, K.L. Yeung, C.Y. Lee, P.L. Yue, C.K. Chan, *J. Catal.* 192 (2000) 185–196.
- L. Zang, W. Macyk, C. Lange, W.F. Maier, C. Antonius, D. Meissner, H. Kisch, *Chem. Eur. J.* 6 (2000) 379–384.
- F. Bosc, D. Edwards, N. Keller, V. Keller, A. Ayral, *Thin Solid Films* 495 (2006) 272–279.
- R. Asahi, T. Morikawa, T. Ohwaki, K. Aoki, Y. Taga, *Science* 293 (2001) 269–271.
- H. Irie, Y. Watanabe, K. Hashimoto, *J. Phys. Chem. B* 107 (2003) 5483–5486.
- Y. Irokawa, T. Morikawa, K. Aoki, S. Kosaka, T. Ohwaki, Y. Taga, *Phys. Chem. Chem. Phys.* 8 (2006) 1116–1121.
- L. Li, J. Gu, Y. Zhang, *Adv. Mater. Res.* 26–28 (2007) 633–636.
- A. Danion, J. Disdier, C. Guillard, F. Abdelmalek, N. Jaffrezic-Renault, *Appl. Catal. B* 52 (2004) 213–223.
- W. Choi, J.Y. Ko, H. Park, J.S. Chung, *Appl. Catal. B* 31 (2001) 209–220.
- S. Horikoshi, N. Watanabe, H. Onishi, H. Hidaka, N. Serpone, *Appl. Catal. B* 37 (2002) 117–129.
- V. Kandavelu, M.R. Dhannanjeyan, R. Renganathan, S.K. Badamali, P. Selvam, *J. Mol. Catal. A* 157 (2000) 189–192.
- R.J. Candal, W.A. Zeltner, M.A. Anderson, *J. Environ. Eng.* 125 (1999) 906–912.
- D. Byun, Y. Jin, B. Kim, J.K. Lee, D. Park, *J. Hazard. Mater.* 73 (2000) 199–206.
- T. Temchenko, R. Marchetti, *A. Surf. Coat. Int.* 81 (1998) 448–450.
- B. Herbig, P. Lobmann, *J. Photochem. Photobiol. A* 163 (2004) 359–365.
- Z. Ding, X. Hu, P.L. Yue, G.Q. Lu, P.P. Greenfield, *Catal. Today* 68 (2001) 173–182.
- F. Toshiaki, O. Hotta, JP Patent 19990602, 1999.
- M.J. Uddin, F. Cesano, F. Bonino, S. Bordiga, G. Spoto, D. Scarano, A. Zecchina, *J. Photochem. Photobiol. A* 189 (2007) 286–294.
- P.-A. Bourgeois, E. Puzenat, L. Peruchon, F. Simonet, D. Chevalier, E. Delfin, C. Brochier, C. Guillard, *Appl. Catal. B* 128 (2012) 171–178.
- R. Pelton, X. Geng, M. Brook, *Adv Colloid Interface Sci.* 127 (2006) 43–53.
- C. Raillard, V. Hequet, P. Le Cloirec, J. Legrand, *J. Photochem. Photobiol. A* 163 (2004) 425–431.
- P. Escaffre, P. Girard, J. Dussaud, L. Bouvier, U.S. patent 6 906 001 B1, 2005.
- C. Guillard, J. Disdier, C. Monnet, J. Dussaud, S. Malato, J. Blanco, M.I. Maldonado, J.-M. Herrmann, *Appl. Catal. B* 46 (2003) 319–332.
- S. Ko, P.D. Fleming, M. Joyce, P. Ari-Gur, Mater. Sci. Eng. B 166 (2010) 127–131.
- S. Ko, P.D. Fleming, M. Joyce, P. Ari-Gur, Mater. Sci. Eng. B 164 (2009) 135–139.
- N. Kimura, S. Abe, T. Yoshimoto, S. Fukayama, U.S. Patent 6 228 480 B1, 2001.
- Y. Iguchi, H. Ichiiura, T. Kitaoka, H. Tanaka, *Chemosphere* 53 (2003) 1193–1199.
- S. Fukahori, Y. Iguchi, H. Ichiiura, T. Kitaoka, H. Tanaka, H. Wariishi, *Chemosphere* 66 (2007) 2136–2141.

- [46] H. Matsubara, M. Takad, S.H. Koyama, K. Hashimoto, A. Fujishima, *Chem. Lett.* (1995) 767–768.
- [47] H. Ichura, T. Kitaoka, H. Tanaka, *Chemosphere* 50 (2003) 79–83.
- [48] F. Amiche, US Patent 6221326B1, 2001.
- [49] P. Nortier, E., Zeno, PCT Int. Appl., WO 2008129197 A2 20081030, 2008.
- [50] J. Allix, M.-C. Angelier, V., Meyer, P., Nortier, E., Zeno, N., Ralhan, V. Jollet, Proceeding 12ème Congrès de la Société Française de Génie des Procédés, (SFGP 2009), France 2009.
- [51] M. Rivalin, M. Benmami, A.V. Kanaev, A. Gaunand, *Chem. Eng. Res. Des.* 83 (2005) 67–74.
- [52] M. Benmami, K. Chhor, A.V. Kanaev, *Chem. Phys. Lett.* 422 (2006) 552–557.
- [53] R. Azouani, A. Michau, K. Hassouni, K. Chhor, J.-F. Bocquet, J.-L. Vignes, A. Kanaev, *Chem. Eng. Res. Des.* 88 (2010) 1123–1130.
- [54] R. Azouani, A. Solov'ev, M. Benmami, K. Chhor, J.-F. Bocquet, A. Kanaev, *J. Phys. Chem. C* 111 (2007) 16243–16248.
- [55] M. Benmami, K. Chhor, A. Kanaev, *J. Phys. Chem. B* 109 (2005) 19766–19771.
- [56] ISO 5269-2, Pulps—Preparation of Laboratory Sheets for Physical Testing—Part 2: Rapid-Köthen Method, 01/11/2004.
- [57] ISO 5264/1, Pulps—Laboratory Beating—Part 1: Valley Beater Method, 15/07/1979.
- [58] ISO 5267/1, Pulps—Determination of Drainability—Schopper-Riegler Method, 01/03/1999.
- [59] TAPPI Test Methods, T 402 sp-03, Standard Conditioning and Testing Atmospheres for Paper, Board, Pulp Handsheets, and Related Products, 2007.
- [60] TAPPI Test Methods, T 211 om-07, Ash in Wood, Pulp, Paper And Paperboard: Combustion at 525 °C, Reaffirmed 2007.
- [61] ISO 536—Paper and Board—Determination of Basis Weight, 1995.
- [62] NF Q03-076-1986, Paper and Board, Determination of Air Permeance, Bendtsen's Method, 01/04/1986.
- [63] CRC Handbook of Chemistry and Physics, D.R. Lide (ed), 84th ed., CRC Press, Boca Raton, 2003–2004.
- [64] ISO 2470-1:2009, Paper, Board and Pulps—Measurement of Diffuse Blue Reflectance Factor—Part 1: Indoor Daylight Conditions (ISO Brightness).
- [65] P. Pucher, M. Benmami, R. Azouani, G. Krammer, K. Chhor, J.-F. Bocquet, A.V. Kanaev, *Appl. Catal. A* 332 (2007) 297–303.
- [66] M. Bouslama, M.C. Amamra, S. Tieng, O. Brinza, K. Chhor, M. Abderrabba, J.-L. Vignes, A. Kanaev, *Appl. Catal. A* 402 (2011) 156–161.
- [67] M. Bouslama, M.C. Amamra, Z. Jia, M. Ben Amar, O. Brinza, K. Chhor, M. Abderrabba, J.-L. Vignes, A. Kanaev, *ASC Catal.* 2 (2012) 1884–1892.
- [68] O. Khatiim, M. Amamra, K. Chhor, T. Bell, D. Novikov, D. Vrel, A. Kanaev, *Chem. Phys. Lett.* 558 (2013) 53–56.
- [69] M. Benmami, Elaboration d'oxyde de titane nanométrique par voie sol-gel: mise en forme et application en photocatalyse, PhD thesis, Université Paris XIII, 2006.
- [70] K. Seonghyuk, J. Pekarovic, P.D. Fleming, A-G. Pnina, *Mater. Sci. Eng. B* 166 (2010) 127–131.
- [71] C. Nguyen Dinh An, Conception et réalisation d'un pilote pour le traitement photocatalytique d'effluent gazeux pollués en composés organiques volatils: Application à l'élimination du méthanol dans l'air, Ph.D. thesis, Institut National Polytechnique de Grenoble, 2001.

Glossary

- B_0 : Air permeability [$\text{mL(STP)}\text{ min}^{-1}$]
 C : Steady-state ethanol concentration [mg m^{-3}]
 C_0 : Ethanol concentration at the paper inlet [mg m^{-3}]
 L : Paper thickness [μm]
 Q : Air flow rate [$\text{cm}^3(\text{STP})\text{ min}^{-1}$]
 S_g : Specific surface [$\text{m}^2\text{ g}^{-1}$]
 U : Axial superficial velocity [m s^{-1}]
 X_{EOH} : Ethanol conversion [–]
 W : TiO_2 loading in the paper sheet [g]

Greek symbols

- ΔP : Pressure difference in Eq. (1) (1.47 kPa)
 μ : Air viscosity [$1.8 \times 10^{-5} \text{ kg m}^{-1} \text{ s}^{-1}$ at 293 K]